Infrared ultrafast spectroscopy of solution-grown thin film tellurium

Vasudevan Iyer,[1] Mauricio Segovia,[1] Yixiu Wang,[2] Wenzhuo Wu,[2] Peide Ye,[3] and Xianfan Xu[1,*]

[1]*School of Mechanical Engineering and Birck Nanotechnology Center, Purdue University, West Lafayette, Indiana 47907, USA*
[2]*School of Industrial Engineering, Purdue University, West Lafayette, Indiana 47907, USA*
[3]*School of Electrical Engineering and Birck Nanotechnology Center, Purdue University, West Lafayette, Indiana 47907, USA*

(Received 15 May 2019; revised manuscript received 7 August 2019; published 28 August 2019)

Several materials studied intensively in their bulk forms several decades ago have re-emerged in recent years in their thin film and monolayer manifestations. Tellurium, like black phosphorus, is one such elemental two-dimensional material with promising semiconducting properties for electronic and optoelectronic applications. To study fundamental carrier properties such as hot carrier relaxation and recombination, we performed ultrafast femtosecond pump-probe spectroscopy on thin flakes of solution-grown tellurium. To access the low band gap of tellurium, we used infrared, near-band-gap and below-band-gap probes to monitor the relaxation processes. Sweeping the probing wavelengths across the band gap helps to shed light on the anisotropic band structure of the material. We find that relaxation in flakes of 60–160 nm thickness is on the order of 100 s of picoseconds. Thinner flakes (10–20 nm), on the other hand, exhibit fast relaxation times of sub-20 ps. Radiative recombination is identified as the relaxation mechanism in thick flakes, whereas midgap trap states arising from surface defects and impurities are responsible for the fast relaxation in thin flakes. A diffusion-recombination model accounting for the surface defect and radiative recombinations explains the experimental data well.

DOI: 10.1103/PhysRevB.100.075436

With ever-increasing demands on the performance, robustness, and speed of electronic and computing devices, there is a search for novel materials to continue the Moore's law into the next decade. To this end, two-dimensional (2D) materials are being intensely studied to ascertain their utility for the next generation of transistors, photodetectors, interconnects, and a host of other components [1–3]. After several successful applications of graphene [4,5], its limited performance in transistors due to lack of band gap [6] has led to the investigation and discovery of many other 2D materials such as transition metal dichalcogenides [7], black phosphorus [8,9], and topological insulators [10]. Even these new materials suffered from some limitations. For example, transition metal dichalcogenides exhibit low electron/hole mobilities in general [11,12], and black phosphorus is unstable in air due to oxidation [13]. The enhanced properties of topological insulator surface states could not be harnessed to their full potential due to bulk contribution [14]. Another major challenge is the fabrication of these 2D materials on a large scale, with extensive efforts being invested in techniques such as chemical vapor deposition [15], molecular beam epitaxy [16], and liquid phase exfoliation [17]. Only a few materials, such as some transition metal dichalcogenides and graphene, are being produced on a wafer scale [18,19].

A recent 2D material, 2D tellurium, has emerged as a promising candidate for electronic and optoelectronic applications. A novel substrate free solution growth method has been developed which facilitates controllable flake thickness [20,21]. Moreover, using the Langmuir-Blodgett process and inkjet printing, the flakes can be assembled to obtain large area samples [20]. Apart from the feasibility of scalable growth, tellurium transistors have been shown to exhibit high mobility, good on/off ratio, and large drain current [20,22–24]. Furthermore, the band gap is thickness tunable, which could prove useful in tunable light absorption [20]. Finally, the material is air stable without the need for encapsulation [20], thus overcoming many of the limitations discussed previously. A more detailed description of the properties of this material can be found in a recent review [25]. Due to rising interest in this material, it is important to understand the fundamental electron/hole carrier dynamics which directly impacts the performance of devices. Ultrafast pump-probe spectroscopy is a useful tool to investigate hot carrier dynamics, carrier scattering, and recombination in a variety of materials such as nanoparticles [26], quantum dots [27], metals [28], and 2D materials [29,30]. There have been ultrafast studies on the coherent phonon dynamics in bulk tellurium crystals [31,32] but no studies on the near-band-gap and free-carrier dynamics on thin films to the best of our knowledge. Since most devices rely on near-band-edge phenomena, it is essential to understand the infrared transient response of the material, which can access the small band gap of 0.35 eV [33].

The tellurium flakes were synthesized using the substrate free solution growth method [20], and the suspended flakes were scooped out from the solution onto a CaF_2 substrate with predeposited gold location markers (see Supplemental Material Note 1 [34]). The flakes were identified with an optical microscope [Fig. 1(a)], followed by collecting a Raman spectrum [Horiba LabRAM, Fig. 1(b)] to determine the flake orientation [20] (see Supplemental Material Note 2 [34] and references [35,36] therein). The red arrow in Fig. 1(a) is the direction perpendicular to the c axis (or parallel to

*xxu@ecn.purdue.edu

 ©2019 American Physical Society

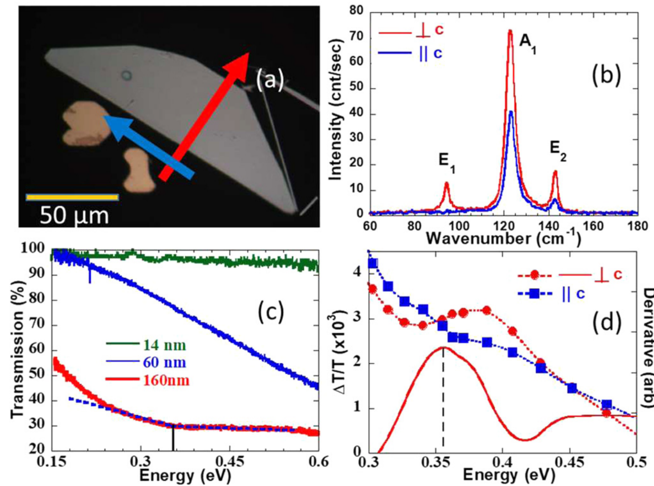

FIG. 1. Characterization of a 130-nm flake using (a) optical microscopy and (b) Raman spectroscopy to determine orientation. (c) FTIR transmission for flakes with various thicknesses. The change in the slope of the curve for the 160-nm flake corresponds to a band gap of 0.35 eV. (d) The change in transmission at the 7-ps delay for a 130-nm flake as a function of energy for pump-and-probe polarizations either oriented perpendicular or parallel to the *c* axis, with spline fits (dotted lines) and its derivative (solid line). The band edge near 0.35 eV is clearly discernable for light polarization perpendicular to the *c* axis.

the [1$\bar{2}$10] axis), and the blue arrow is parallel to the *c* axis ([0001] axis). An atomic force microscopy (AFM) scan was done to determine the thickness. Fourier-transform infrared (FTIR) spectroscopy transmission scans were also performed using an FTIR microscope (Thermo Fisher Scientific, Continuum) as shown in Fig. 1(c) for three flakes of thickness 14, 60, and 160 nm. The point where the slope changes in the 160-nm flake, indicated by the intersected straight line in Fig. 1(c), corresponds to a band gap of 0.35 eV. The 14-nm flake shows weak humplike features near 0.3 eV, which could be due to many-body effects such as excitons. A recent study theoretically predicted exciton binding energy of up to 670 meV in monolayer suspended tellurium and decreased strength for supported samples and thicker films [37]. Detailed thickness-dependent photoluminescence excitation spectroscopy [38,39] could reveal more details and is beyond the scope of this work. Bulk flakes were predicted to have <10 meV binding energy at room temperature, and hence we have neglected excitonic effects in our analysis for >20-nm flakes. More discussion on <20-nm samples will be provided later. Ultrafast pump-probe transmission spectroscopy was carried out on the flakes (see Supplemental Material Note 3 [34], for experimental details). The change in transmission ($\Delta T/T$) at a pump-and-probe delay time of 7 ps for a 130-nm flake, with the probe wavelength varying across the band gap, is shown in Fig. 1(d). The pump and probe were both either polarized along the *c* axis ($\|c$) or perpendicular to the *c* axis ($\perp c$). The transmission data for light polarization perpendicular to the *c* axis is more indicative to the band gap, as has been observed previously in literature for bulk crystal [33]. The photogenerated carriers accumulate near the band edge; hence there is a larger change in the transmission of the probe when its wavelength is tuned close to the band gap. The change of transmission vs wavelength can be seen more clearly by fitting a spline curve through the experimental data points and performing a numerical differentiation [40] to obtain the point of maximum, which is indicated by the black dashed line at 0.355 eV. The pump and probe were polarized perpendicular to the *c* axis in the remainder of the manuscript.

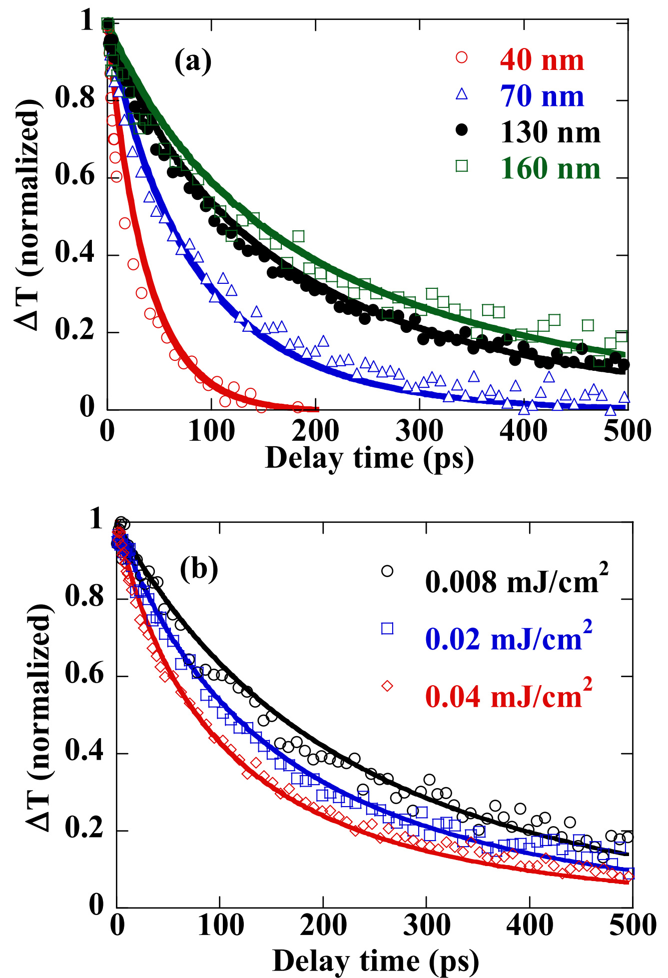

FIG. 2. (a) Relaxation dynamics in 40–160 nm flakes following excitation by 800-nm pump and probing with 3500 nm. The transient curves are normalized, and the point of maximum signal is set as a delay time of 0 ps. The solid lines are obtained from diffusion-recombination model simulations. (b) Fluence-dependent measurements on a 130-nm flake along with simulation curves.

The relaxation dynamics of 40–160-nm flakes following excitation by the 800-nm (1.55-eV) pump beam is shown in Fig. 2(a) for a band-edge probe wavelength of 3500 nm (0.35 eV). The pump fluence is 0.02 mJ/cm^2. Results with a 5800-nm (0.21-eV) probe are provided in Supplemental Material Note 4 [34], Fig. S1. Fluence-dependent dynamics for a 130-nm flake are shown in Fig. 2(b). The recombination dynamics in tellurium has been studied previously using steady-state [41] and transient photoconductivity [42], as well as transient microwave conductivity [43]. These studies did not have the time resolution to determine the recombination time at room temperature. The reported values at low

temperature (77 K) range in the 10s of nanoseconds to microsecond regime, and the authors predicted the room-temperature recombination time to be several orders smaller than at low temperature. A recent study on recombination dynamics in powdered tellurium obtained a few nanosecond lifetimes at room temperature using transient microwave conductivity with a minimum time resolution of 300 ps [44]. Our measurements are the first on thin film tellurium with subpicosecond time resolution.

A diffusion-recombination model (see Supplemental Material Note 5 [34], and Ref. [45] therein) was used to simulate the dynamics as shown by the solid lines in Figs. 2(a) and 2(b). Several recombination mechanisms have been proposed for bulk tellurium in literature, such as direct recombination [41], trap/defect states near the band edge [42], midgap trap states [43], and point defects and dislocations [46]. The transmission electron microscopy (TEM) cross section of the flakes in a previous study revealed good quality of the flakes in the bulk, and hence point defects and dislocations are less likely [20]. Therefore, radiative or SRH (Shockley-Read-Hall, trap-assisted) recombination are the more probable recombination routes, as was also deduced in a recent study on recombination dynamics in powdered tellurium [44]. Moreover, the authors found that radiative recombination is dominant with 98% radiative yield at room temperature. Hence, we modeled the dynamics with radiative recombination (which accounts for the fluence dependence), surface recombination (which accounts for the thickness dependence), and the diffusion process. By fitting the radiative recombination coefficient and surface recombination term, we obtained good agreements with experiments, as seen in Figs. 2(a) and 2(b) for both thickness-dependent and fluence-dependent data. The radiative recombination coefficient was obtained as $1.9 \mp 0.1 \times 10^{-9}\,\text{cm}^3/\text{s}$. Our value is lower than the $1.1 \times 10^{-8}\,\text{cm}^3/\text{s}$ obtained by Bhaskar *et al.* [44] but higher than other traditional direct-band-gap semiconductors such as GaAs, which has a value of $\sim 7 \times 10^{-10}\,\text{cm}^3/\text{s}$ at room temperature. The surface recombination velocity is found as $V_s = \frac{2\times10^6}{t}$ cm/s, where t is the thickness in nanometers. Typically, the Fuchs-Sondheimer theory is used to account for the thickness-dependent electrical resistivity, which has a $\sim 1/t$ dependence for $t \gg \lambda$, where λ is the mean free path [47,48]. The $1/t$ trend obtained from our modeling is likely a lumped effect from a number of phenomena, such as scattering and possible thickness-dependent surface defects.

Flakes with smaller thicknesses show different dynamics, and a transition occurs at around 40-nm thickness as shown in Fig. 3(a). The sign of the transmission signal starts flipping from positive to negative accompanied by a shorter time constant of decay. Comparing the 3500-nm probe and 5800-nm probe for the 40-nm flake, we see that after the change in sign from negative to positive for the 5800-nm probe, the curves merge at about 50 ps. This shows that there are two distinct relaxation processes. As the thickness is reduced further, the signs for both probe wavelengths become negative and the lifetime is sub-20 ps, as seen in Fig. 3(b) for a 12-nm flake with a 3500-nm probe. (A 5800-nm probe, shown in Supplemental Material Note 4, Fig. S2 [34], produces a very similar result.) The simulation reproduces the fast relaxation well, as shown by the blue solid line in Fig. 3(b). Two

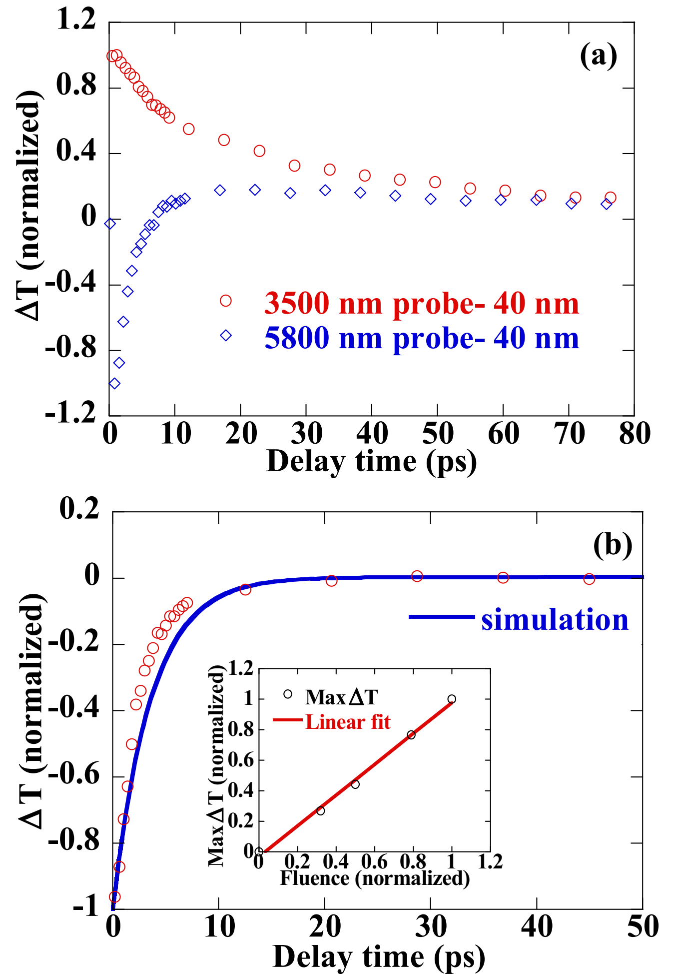

FIG. 3. (a) Relaxation dynamics in a 40-nm-thick flake showing positive sign (3500 nm probe) and sign flipping (5800-nm probe). At delays greater than 50 ps, the curves merge together. (b) Relaxation dynamics in a 12-nm flake following excitation by an 800-nm pump and probing with 3500 nm. Inset shows pump fluence dependence along with linear fit, confirming the absence of any nonlinear effects. The blue solid line is from the diffusion-recombination simulation.

more flakes with thickness 13 and 17 nm produced similar results.

In thinner flakes, the observed relaxation is entirely due to carrier capture by surface trap states. The mobility of transistors made from solution-grown tellurium was seen to sharply decrease below 20 nm thickness [20] and was ascribed to surface scattering and interface defects. Such time scales have been previously related to fast capture of carriers by midgap defect states in MoS_2 [49]. To ensure that the drastic change in the signal is not due to nonlinear effects such as Auger recombination, we show the maximum change in transmission as a function of fluence and observe a linear trend as shown in the inset of Fig. 3(b), which rules out such possibilities. A fluence test of relaxation time (Supplemental Material Note 6, Fig. S4 [34]) revealed fluence-independent relaxation, which further suggests surface recombination as the dominant mechanism in thin flakes.

We also address the thickness dependence of the band gap, as it is known to increase from bulk to monolayer [20]. The

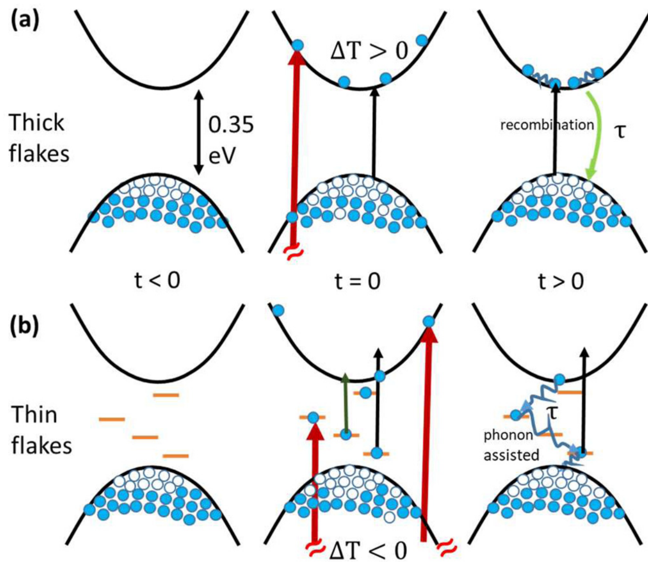

FIG. 4. Excitation and relaxation mechanism in thick flakes (upper three panels), where direct recombination plays a dominant role, and in thin flakes (10–20 nm, lower three panels), where the excited carriers recombine predominantly through several midgap surface trap states. The red arrow denotes the pump beam (800 nm), the black and dark green arrows represent the 3500- and 5800-nm probe, respectively. The white circles are the holes and blue circles are the electrons. The orange bars are trap states.

12-nm flake, for example, is expected to show an increase of ∼50 meV and have a band gap of ∼0.4 eV. We measured the dynamics with a 2800-nm (0.44 eV) probe but did not observe any difference compared to the 3500-nm (0.35-eV) probe (Supplemental Material Note 7, Fig. S5 [34]). We also performed a probe wavelength sweep near a time delay of 0 ps (Supplemental Material Note 7, Fig. S6 [34]) and found only weak features similar to the FTIR spectrum shown in Fig. 1(c) for a 14-nm flake. Hence, we conclude that either the band gap did not change as predicted or that the 3500-nm probe monitors the free carriers and hence does not show any difference compared to the near-band-gap probe of 2800 nm, similar to probing with a 5800-nm probe. Excitonic effects could play a role in the thin films as discussed previously; however, the exciton lifetimes are generally in the hundreds of picoseconds to nanoseconds range [50–52], unlike the short time scales in our measurements. Some studies found the lifetime to be <10 ps at very low temperature of 4 K, but hundreds of picoseconds at room temperature [53,54]. Furthermore, time scales of <5 ps at room temperature were attributed to trapping of excitons by surface defects in MoS_2 [55]. Therefore, we conclude that even with possible exciton activity for the thin flakes, the surface-defect-assisted relaxation is the dominant process at room temperature.

The excitation and recombination processes can be summarized in Fig. 4. Figure 4(a) describes thick flakes and Fig. 4(b) describes thin flakes. Before the arrival of the pump pulse ($t < 0$, left column), the material is at its ground state (p type [20]). At the time of excitation ($t = 0$, center column), the pump pulse finishes populating the higher-energy states, i.e., the conduction band in the thick flakes and both conduction band and midgap trap states in the thin flakes. An intraband thermalization process (on the order of 100 fs in common 2D materials [56,57]) occurs within the time resolution of our experiment (500 fs). After rapid carrier-phonon scattering, carrier recombination occurs. In case of thin flakes, since the recombination proceeds through the many midgap trap states, it must necessarily be phonon assisted as shown, which explains why the recombination time is on the order of the electron-phonon interaction times.

The proposed ultrafast transmission mechanisms in Fig. 4 also explain the increased or decreased transmission in thick and thin flakes. The positive sign of the transmission signal (induced transmission) in thick flakes indicates Pauli blocking between initial and final states, thus indicating interband probing as shown in Fig. 4(a). The 3500-nm probe monitors the valence band to conduction band transition, whereas the 5800-nm probe monitors intervalence band transitions, several of which, in the midinfrared region, have been found in literature [20,58–61]. On the other hand, thin flakes show a negative transmission signal (induced absorption), thereby indicating transitions from midgap trap states to the conduction band as shown in Fig. 4(b). For the transition flake [40-nm flake, Fig. 3(a)], the negative signal from the midgap trap states and the positive signal from the Pauli blocking start to compete. The 3500-nm probe response is dominated by interband transition due to it being the primary strong transition, whereas the 5800-nm probe starts to encounter a superposition of responses from intervalence band states and midgap trap states, producing a sign change.

Finally, we looked at the transient dynamics with pump-and-probe polarizations in the direction parallel to the c axis. The absorption coefficient of the pump laser is different along the c axis and perpendicular to it by a factor of 1.8 for the 130-nm flake (see Supplemental Material Note 3 [34]), and hence pumping and probing along the c axis should produce a change in the slope of the relaxation due to different initial exited carrier concentrations. We observe such a dependence as shown in Supplemental Material Note 8, Fig S7 [34]. The thinner flakes did not show any directional dependence and reinforce the fluence-independent surface recombination mechanism as shown in Supplemental Material Note 8, Fig. S8 [34].

In summary, we have performed ultrafast infrared transmission spectroscopy on tellurium flakes with thicknesses ranging from 12 to 160 nm and found a strong dependence of the recombination times on thickness. Thin flakes show a fast decay on the order of 20 ps, whereas thicker flakes have a decay in the hundreds of picoseconds range. The recombination mechanism in thin flakes was attributed to fast carrier capture by midgap defect states arising from surface defects and that in the thick flakes to radiative recombination. Recombination coefficients were extracted using a diffusion-recombination model. The fundamental carrier dynamics for tellurium thin films at room temperature aids in the understanding and better design of electronic and optoelectronic devices.

We acknowledge financial support from AFOSR/NSF under EFRI2- DARE Grant No. EFMA-1433459 and NSF Grant No. CMMI-1762698. We also thank Shouyuan Huang for preparing CaF_2 substrates.

[1] G. Fiori, F. Bonaccorso, G. Iannaccone, T. Palacios, D. Neumaier, A. Seabaugh, S. K. Banerjee, and L. Colombo, Nat. Nanotechnol. **9**, 768 (2014).

[2] N. Briggs, S. Subramanian, Z. Lin, X. Li, X. Zhang, K. Zhang, K. Xiao, D. Geohegan, R. Wallace, L.-Q. Chen, M. Terrones, A. Ebrahimi, S. Das, J. Redwing, C. Hinkle, K. Momeni, A. van Duin, V. Crespi, S. Kar, and J. A. Robinson, 2D Mater. **6**, 022001 (2019).

[3] P. K. Venuthurumilli, P. D. Ye, and X. Xu, ACS Nano **12**, 4861 (2018).

[4] Q. Bao and K. P. Loh, ACS Nano **6**, 3677 (2012).

[5] P. Avouris, Nano Lett. **10**, 4285 (2010).

[6] F. Schwierz, Nat. Nanotechnol. **5**, 487 (2010).

[7] Q. H. Wang, K. Kalantar-Zadeh, A. Kis, J. N. Coleman, and M. S. Strano, Nat. Nanotechnol. **7**, 699 (2012).

[8] H. Liu, A. T. Neal, Z. Zhu, Z. Luo, X. Xu, D. Tománek, and P. D. Ye, ACS Nano **8**, 4033 (2014).

[9] F. Xia, H. Wang, and Y. Jia, Nat. Commun. **5**, 4458 (2014).

[10] Y. L. Chen, J. G. Analytis, J.-H. Chu, Z. K. Liu, S.-K. Mo, X. L. Qi, H. J. Zhang, D. H. Lu, X. Dai, Z. Fang, S. C. Zhang, I. R. Fisher, Z. Hussain, and Z.-X. Shen, Science **325**, 178 (2009).

[11] L. Cheng and Y. Liu, J. Am. Chem. Soc. **140**, 17895 (2018).

[12] Z. Yu, Z.-Y. Ong, S. Li, J.-B. Xu, G. Zhang, Y.-W. Zhang, Y. Shi, and X. Wang, Adv. Funct. Mater. **27**, 1604093 (2017).

[13] J. O. Island, G. A. Steele, H. S. J. van der Zant, and A. Castellanos-Gomez, 2D Mater. **2**, 011002 (2015).

[14] C. Durand, X.-G. Zhang, S. M. Hus, C. Ma, M. A. McGuire, Y. Xu, H. Cao, I. Miotkowski, Y. P. Chen, and A.-P. Li, Nano Lett. **16**, 2213 (2016).

[15] A. Reina, X. Jia, J. Ho, D. Nezich, H. Son, V. Bulovic, M. S. Dresselhaus, and J. Kong, Nano Lett. **9**, 30 (2009).

[16] A. Roy, H. C. P. Movva, B. Satpati, K. Kim, R. Dey, A. Rai, T. Pramanik, S. Guchhait, E. Tutuc, and S. K. Banerjee, ACS Appl. Mater. Interfaces **8**, 7396 (2016).

[17] J. Kang, J. D. Wood, S. A. Wells, J.-H. Lee, X. Liu, K.-S. Chen, and M. C. Hersam, ACS Nano **9**, 3596 (2015).

[18] Y.-C. Lin, W. Zhang, J.-K. Huang, K.-K. Liu, Y.-H. Lee, C.-T. Liang, C.-W. Chu, and L.-J. Li, Nanoscale **4**, 6637 (2012).

[19] Y. Lee, S. Bae, H. Jang, S. Jang, S.-E. Zhu, S. H. Sim, Y. Il Song, B. H. Hong, and J.-H. Ahn, Nano Lett. **10**, 490 (2010).

[20] Y. Wang, G. Qiu, R. Wang, S. Huang, Q. Wang, Y. Liu, Y. Du, W. A. Goddard, M. J. Kim, X. Xu, P. D. Ye, and W. Wu, Nat. Electron. **1**, 228 (2018).

[21] Y. Wang, R. de Souza Borges Ferreira, R. Wang, G. Qiu, G. Li, Y. Qin, P. D. Ye, A. Sabbaghi, and W. Wu, Nano Energy **57**, 480 (2019).

[22] M. Amani, C. Tan, G. Zhang, C. Zhao, J. Bullock, X. Song, H. Kim, V. R. Shrestha, Y. Gao, K. B. Crozier, M. Scott, and A. Javey, ACS Nano **12**, 7253 (2018).

[23] S. Berweger, G. Qiu, Y. Wang, B. Pollard, K. L. Genter, R. Tyrrell-Ead, T. M. Wallis, W. Wu, P. D. Ye, and P. Kabos, Nano Lett. **19**, 1289 (2019).

[24] G. Qiu, Y. Wang, Y. Nie, Y. Zheng, K. Cho, W. Wu, and P. D. Ye, Nano Lett. **18**, 5760 (2018).

[25] W. Wu, G. Qiu, Y. Wang, R. Wang, and P. Ye, Chem. Soc. Rev. **47**, 7203 (2018).

[26] C. Chen, I. Vasudevan, Z. Du, X. Xu, and L. Pan, Appl. Phys. Lett. **112**, 253105 (2018).

[27] B. T. Spann and X. Xu, Appl. Phys. Lett. **105**, 083111 (2014).

[28] L. Guo and X. Xu, J. Heat Transfer **136**, 122401 (2014).

[29] F. Ceballos and H. Zhao, Adv. Funct. Mater. **27**, 1604509 (2017).

[30] V. Iyer, Y. P. Chen, and X. Xu, Phys. Rev. Lett. **121**, 026807 (2018).

[31] S. Hunsche, K. Wienecke, T. Dekorsy, and H. Kurz, Phys. Rev. Lett. **75**, 1815 (1995).

[32] N. Kamaraju, S. Kumar, M. Anija, and A. K. Sood, Phys. Rev. B **82**, 195202 (2010).

[33] S. Tutihasi, G. G. Roberts, R. C. Keezer, and R. E. Drews, Phys. Rev. **177**, 1143 (1969).

[34] See Supplemental Material at http://link.aps.org/supplemental/10.1103/PhysRevB.100.075436 for details of the material synthesis, Raman characterization, experimental setup, simulation, and additional experiments.

[35] A. S. Pine and G. Dresselhaus, Phys. Rev. B **4**, 356 (1971).

[36] R. M. Martin, G. Lucovsky, and K. Helliwell, Phys. Rev. B **13**, 1383 (1976).

[37] Y. Pan, S. Gao, L. Yang, and J. Lu, Phys. Rev. B **98**, 085135 (2018).

[38] H. M. Hill, A. F. Rigosi, C. Roquelet, A. Chernikov, T. C. Berkelbach, D. R. Reichman, M. S. Hybertsen, L. E. Brus, and T. F. Heinz, Nano Lett. **15**, 2992 (2015).

[39] K. Yao, A. Yan, S. Kahn, A. Suslu, Y. Liang, E. S. Barnard, S. Tongay, A. Zettl, N. J. Borys, and P. J. Schuck, Phys. Rev. Lett. **119**, 087401 (2017).

[40] A. Ferreira da Silva, N. Veissid, C. Y. An, I. Pepe, N. Barros de Oliveira, and A. V. Batista da Silva, Appl. Phys. Lett. **69**, 1930 (1996).

[41] D. Redfield, Phys. Rev. **100**, 1094 (1955).

[42] V. A. Vis, J. Appl. Phys. **35**, 360 (1964).

[43] A. Bringer and G. Nimtz, Phys. Status Solidi **46**, 235 (1971).

[44] P. Bhaskar, A. W. Achtstein, M. J. W. Vermeulen, and L. D. A. Siebbeles, J. Phys. Chem. C **123**, 841 (2019).

[45] S. M. Sze and K. K. Ng, *Physics of Semiconductor Devices* (John Wiley & Sons, Hoboken, NJ, 2006).

[46] J. S. Blakemore, J. W. Schultz, and K. C. Nomura, J. Appl. Phys. **31**, 2226 (1960).

[47] E. H. Sondheimer, Adv. Phys. **1**, 1 (1952).

[48] F. Lacy, Nanoscale Res. Lett. **6**, 636 (2011).

[49] H. Wang, C. Zhang, and F. Rana, Nano Lett. **15**, 339 (2015).

[50] L. Yuan and L. Huang, Nanoscale **7**, 7402 (2015).

[51] T. Wang, Y. Zhang, Y. Liu, J. Li, D. Liu, J. Luo, and K. Ge, J. Phys. Chem. C **122**, 18651 (2018).

[52] N. Kumar, Q. Cui, F. Ceballos, D. He, Y. Wang, and H. Zhao, Nanoscale **6**, 4915 (2014).

[53] T. Korn, S. Heydrich, M. Hirmer, J. Schmutzler, and C. Schüller, Appl. Phys. Lett. **99**, 102109 (2011).

[54] C. Robert, D. Lagarde, F. Cadiz, G. Wang, B. Lassagne, T. Amand, A. Balocchi, P. Renucci, S. Tongay, B. Urbaszek, and X. Marie, Phys. Rev. B **93**, 205423 (2016).

[55] H. Shi, R. Yan, S. Bertolazzi, J. Brivio, B. Gao, A. Kis, D. Jena, H. G. Xing, and L. Huang, ACS Nano **7**, 1072 (2013).

[56] J. M. Dawlaty, S. Shivaraman, M. Chandrashekhar, F. Rana, and M. G. Spencer, Appl. Phys. Lett. **92**, 042116 (2008).

[57] Z. Nie, R. Long, L. Sun, C. C. Huang, J. Zhang, Q. Xiong, D. W. Hewak, Z. Shen, O. V. Prezhdo, and Z. H. Loh, ACS Nano **8**, 10931 (2014).

[58] E. Bangert, D. Fischer, and P. Grosse, Phys. Status Solidi **59**, 419 (1973).

[59] D. Fischer, E. Bangert, and P. Grosse, Phys. Status Solidi **55**, 527 (1973).

[60] R. Enderlein and A. Hache, Phys. Status Solidi **60**, 739 (1973).

[61] J. Qiao, Y. Pan, F. Yang, C. Wang, Y. Chai, and W. Ji, Sci. Bull. **63**, 159 (2018).